RSC Advances

PAPER

View Article Online
View Journal | View Issue

Cite this: *RSC Adv.*, 2023, **13**, 7597

Development of $NaY_9Si_6O_{26}:Yb^{3+}$ phosphors with high thermal stability for NIR anti-counterfeiting: study of its crystal structure and luminescent properties

Tae Wook Kang,†[a] Yeon Bin Choi,†[a] Chae Ha Kang,[a] Young Ji Park,[a] Jin Ho Kim,[a] Byungseo Bae *[b] and Sun Woog Kim *[a]

Received 20th January 2023
Accepted 27th February 2023

DOI: 10.1039/d3ra00427a

rsc.li/rsc-advances

Near-infrared (NIR) radiation has generated considerable industrial and research interest. However, NIR phosphors for this are limited by low quantum efficiency and broad spectra. Rare-earth-containing compounds doped with activators as host systems for NIR phosphors may resolve these limitations. Yb^{3+}-doped $NaY_9Si_6O_{26}$ phosphors were synthesized using a conventional solid-state reaction method. The main phase of the synthesized phosphor samples exhibited a hexagonal structure $NaY_9Si_6O_{26}$ phase, and had an angular-shape with an average grain size of 1–3 μm. The $NaY_9Si_6O_{26}:Yb^{3+}$ phosphors showed a near-infrared emission from 950 to 1100 nm, which was attributed to the $^2F_{5/2} \rightarrow {}^2F_{7/2}$ transition of Yb^{3+} ions under 270 and 920 nm excitation. The excitation spectra, recorded by monitoring the emission at 985 nm, showed two bands in the ultraviolet and infrared regions, which correspond to the charge transfer transition and the $^2F_{7/2} \rightarrow {}^2F_{5/2}$ transition of Yb^{3+} ions. At 300 °C, the emission intensity of the $NaY_9Si_6O_{26}:Yb^{3+}$ phosphor remained constant at 82%. Furthermore, the thermal degradation was negligible after cooling, suggesting the possibility of application in advanced anti-counterfeiting applications.

Introduction

Since its discovery, near-infrared (NIR) radiation has attracted considerable industrial and research interest. This type of radiation has promising potential for varied applications, mostly related to the characterization of chemicals, security, pharmaceutical, medical, cosmetic, food, and agricultural industries, which contribute to the continued advancement of modern technology.[1–5] Radiation sources such as tungsten halogen lamps, NIR light-emitting diodes (LEDs), and phosphor-converted LEDs (pc-LEDs) can emit in the infrared range.[6] However, the selection of these radiation sources for varied applications is based on the wavelength, full width at half maximum (FWHM), lifetime, efficiency, and thermal stability. For commercial applications, considering the manufacturing cost and size of radiation sources is essential. Conventional NIR tungsten halogen lamps have low efficiency, a large size, high thermal effect, and short lifetimes.[7] NIR LEDs also do not meet the commercial requirements owing to their narrow FWHM.[8,9] NIR pc-LEDs, conversely, are considered the most suitable light sources because they provide suitable emission, high efficiency, a long lifetime, and excellent durability.[10] Therefore, pc-LEDs are highly preferred alternative radiation sources for NIR applications in devices such as automotive sensors, security applications, remote controls, and spectrometers.[11–13] In recent years, the limitations associated with NIR phosphors, including low quantum efficiency and broad spectra, have been extensively studied.[14–17]

Yb^{3+} has been widely investigated as a simple electronic structure with two multiplets: the $^2F_{5/2}$ level in the excited state and $^2F_{7/2}$ level in the ground state. In recent years, numerous studies have been conducted on the development of Yb^{3+}-doped inorganic materials, and their potential use in optical materials such as lasers,[18] solar cells,[19,20] upconversion phosphors,[21–23] and biological applications.[24] Rare-earth-containing compounds have been studied as host systems for NIR phosphors because of their large stokes shifts and emission with doped activators. Among them, compounds with an apatite structure (space group $P6_3/m$) have been extensively investigated as effective hosts for luminous materials owing to their excellent chemical stability and high efficiency for activated ions.[25–27] $NaY_9Si_6O_{26}$ is a type of oxyapatite compound, $M_{10}(AO_4)_6B_2$ (M = Ca, Ba, La, Y, …; A = P, Si, …; B = F, Cl, OH, …), which has two types of Y^{3+} lattice sites (Wyckoff 4f and 6h).[28]

[a]*Advanced Materials Convergence R&D Division, Display Materials Center, Korea Institute of Ceramic Engineering and Technology, Jinju 52851, Korea. E-mail: skim80@kicet.re.kr*

[b]*Advanced Resources Team, Yeongwol Industrial Promotion Agency, 21-28 Palgoe 1 Nonggongdanji, Yeongwolgun, 26240, Korea*

† These authors contributed equally to this work.

In the present study, a new NIR phosphor Yb^{3+}-doped $NaY_9Si_6O_{26}$ was synthesized using a solid-state reaction, and their crystal structures were identified using Rietveld refinement. The addition of an excess amount of Na_2CO_3 as a raw material results in a drastic increase in the ratio of the $NaY_9Si_6O_{26}$ phase. As a result, a compound close to a single phase was obtained. The synthesized $NaY_9Si_6O_{26}$:Yb^{3+} phosphor had an angular shape with an average grain size of 1–3 μm. The emission and excitation properties of $NaY_9Si_6O_{26}$:Yb^{3+} phosphor were investigated to obtain a better understanding of its thermal stability.

Experimental

Yb^{3+}-doped $NaY_9Si_6O_{26}$ phosphors were synthesized using a conventional solid-state reaction. In the powdered form, Na_2CO_3 (Junsei Chemical Co., Ltd, 99%), Y_2O_3 (Daejung Chemical & Metal Co., Ltd, 99%), SiO_2 (Junsei Chemical Co., Ltd, 99%), and Yb_2O_3 (Wako, 99.9%) were used as starting materials to synthesize $NaY_9Si_6O_{26}$:Yb^{3+} phosphor. The amount of Yb^{3+} was adjusted between 1 and 15 mol% in the Yb^{3+}-doped $NaY_9Si_6O_{26}$ phosphor. Using an agate mortar, these raw materials were mixed in a nonstoichiometric ratio of 30 mol% with an excess of Na_2CO_3 as the chemical parameter for the single phase. For 8 h, the mixture was sintered at 1400 °C. After sintering, the samples were ground using an agate mortar.

The crystal structures of the synthesized powder samples were identified using X-ray powder diffraction (XRD, Bruker D8 Advance). Rietveld analysis using the RIETAN-FP package was carried out to obtain detailed crystallographic data. The morphology of the powder was characterized by scanning electron microscopy (SEM, JEOL, JSM6700F). Photoluminescence emission (PL) and excitation (PLE) spectra were measured at room temperature using a fluorescence spectrophotometer (PSI, DARSA PRO 3400). The PL spectra of $NaY_9Si_6O_{26}$:Yb^{3+} phosphor were obtained under 270 and 920 nm excitation, and the PLE spectra were recorded under 985 nm emission. Temperature-dependent PL spectra were measured in the temperature range 25–300 °C as appropriate.

Results and discussion

Fig. 1(a) shows the XRD patterns of the synthesized $NaY_9Si_6O_{26}$:Yb^{3+} phosphors with an excess amount of Na_2CO_3 as raw material. $NaY_9Si_6O_{26}$:Yb^{3+} was synthesized with a large amount of yttrium silicate impurities in a sample synthesized by stoichiometric mixing without the addition of Na_2CO_3. Yttrium silicate impurities are formed by the remaining Y and Si due to the volatilization behaviour of Na_2CO_3 raw material during sintering. The amount of impurities decreased with an increase in the amount of excess of Na_2CO_3. The sample with the least amount of impurities was synthesized at the addition of 30 mol% Na_2CO_3, and the impurities increased when more than 40 mol% Na_2CO_3 was added. The Rietveld refinement results for the XRD data of $Na(Y_{0.9}Yb_{0.1})_9Si_6O_{26}$ phosphor are shown in Fig. 1(b). The refined crystallographic data and parameters of the XRD patterns of $Na(Y_{0.9}Yb_{0.1})_9Si_6O_{26}$ phosphor are

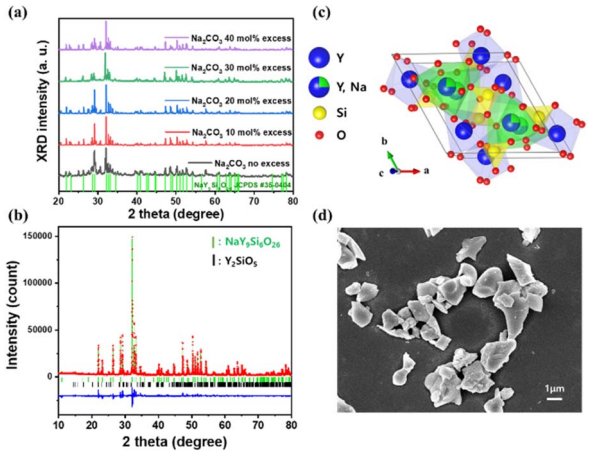

Fig. 1 (a) XRD patterns of $Na(Y_{0.9}Yb_{0.1})_9Si_6O_{26}$ phosphor with excess of Na_2CO_3, (b) Rietveld refinement result for X-ray powder diffraction data of $Na(Y_{0.9}Yb_{0.1})_9Si_6O_{26}$ [red symbol: measured pattern, green solid line: calculated pattern, blue solid line: the difference between their intensities], (c) schematic of the $NaY_9Si_6O_{26}$ crystal structure, (d) SEM images of $NaY_9Si_6O_{26}$:Yb^{3+} phosphor.

summarized in Table 1. The data from the Joint Committee on Powder Diffraction Standards (JCPDS No. 35-0404) corresponding to the $NaY_9Si_6O_{26}$ phase with hexagonal structure obtained were used as the starting model. As shown in Table 1, the final *R*-factor values, R_{wp}, R_p, and S, converged to 5.84, 4.08, and 3.20%, respectively, which verifies the phase purity of the as-prepared sample. The XRD pattern of $Na(Y_{0.9}Yb_{0.1})_9Si_6O_{26}$ indexed mostly with the reported data, and also detected the presence of a small amount of Y_2SiO_5 impurity phase, which accounted for 6%. The final refined $Na(Y_{0.9}Yb_{0.1})_9Si_6O_{26}$ phase was hexagonal in the space group $P6_3/m$ (No. 176) with refined lattice parameters $a = b = 0.93386(0)$ nm, $c = 0.67562(0)$ nm, and $V = 0.58920$ nm^3. Fig. 1(c) shows a schematic of the $NaY_9Si_6O_{26}$ crystal structure produced using VESTA,[29] which corresponds to the apatite structure with two other Y^{3+} sites: Wyckoff 4f and 6h.[28] The Y^{3+} situated at the 6h site (Y1) was surrounded by seven oxygen atoms, whereas the Na^+ and Y^{3+} situated at the 4f sites (Y2) were coordinated by nine oxygen atoms. Simultaneously, the Si^{4+} ion was 4-fold coordinated by

Table 1 Refined crystallographic data for $Na(Y_{0.9}Yb_{0.1})_9Si_6O_{26}$ sample. Hexagonal, space group $P6_3/m$, $a = 0.93386(0)$ nm, $b = 0.93386$ nm, $c = 0.67562(0)$ nm, $R_{wp} = 5.84\%$, $R_p = 4.08\%$, $S = 3.20\%$, $d_1 = 0.3295$, and $d_2 = 0.6511$

Atom	Site	Occ.	*x*	*y*	*z*	$B_{eq.}$
Y1	6h	0.85	0.23336	0.23788	0.25	0.5
Yb1	6h	0.15	0.23336	0.23788	0.25	0.5
Y2	4f	0.75	0.33333	0.66667	0.49888	0.5
Na1	4f	0.25	0.33333	0.66667	0.49888	0.5
Si1	6h	1	0.39760	0.02662	0.25	0.5
O1	2a	1	0.0	0.0	0.25	0.5
O2	6h	1	0.59474	0.12790	0.25	0.5
O3	6h	1	0.33109	−0.15883	0.25	0.5
O4	12i	1	0.33882	0.08590	0.06434	0.5

four oxygen atoms to form a tetrahedron. The ionic radii of 7-coordinated Y^{3+} and Yb^{3+} were calculated to be 0.0960 and 0.0925 nm, respectively, whereas those of 9-coordinated Y^{3+} and Yb^{3+} were calculated to be 0.1075 and 0.1042 nm, respectively. Therefore, based on their similar ionic radii and identical valences, the Yb^{3+} ions were expected to substitute the Y^{3+} lattices in the $NaY_9Si_6O_{26}$ crystal structure. The shapes of $NaY_9Si_6O_{26}$:Yb^{3+} phosphors measured by SEM are shown in Fig. 1(d). The phosphor powder particles were composed of angular-shaped fine grains with an average size of 1–3 μm.

Fig. 2 shows the XRD patterns of $NaY_9Si_6O_{26}$:Yb^{3+} phosphors with varying concentrations. The XRD peaks of all the samples were almost identical to those of the $NaY_9Si_6O_{26}$ phase (JCPDS No. 35-0404), which had hexagonal structure with space group $P6_3/m$. As the Yb^{3+} ion concentration in the $NaY_9Si_6O_{26}$:Yb^{3+} phosphors increased, a peak shift to a higher diffraction angle was observed because Y^{3+} ions (ionic radius: 0.0960 nm for 7 coordination) in the host material were partially substituted with smaller Yb^{3+} ions (ionic radius: 0.0925 nm for 7 coordination) to form a solid solution.

The excitation and emission spectra of $NaY_9Si_6O_{26}$:Yb^{3+} phosphors with varying concentrations of Yb^{3+} ions are shown in Fig. 3. The PLE spectra recorded by monitoring the emission at 985 nm exhibited a excitation band from 220 to 300 nm. A peak was observed at 270 nm in the ultraviolet region owing to the charge transfer transition, which involves transfer of electrons from the ligand anion O^{2-} to the central cation Yb^{3+} ion.[30] The PL spectra of the $NaY_9Si_6O_{26}$:Yb^{3+} phosphors recorded under 270 nm excitation showed a strong NIR emission band in the range 950–1100 nm, which corresponds to the $^2F_{5/2} \rightarrow {}^2F_{7/2}$ spin-allowed transitions of Yb^{3+} ions. The simple $4f^{13}$ electron configuration of Yb^{3+} has a unique spectral term with two multiplets: ground state multiplets $^2F_{7/2}$ and excited state multiplets $^2F_{5/2}$. Variation in the splitting of the Stark level of Yb^{3+} ions was observed because of the differences in the local crystal fields. The ground state, $^2F_{7/2}$ splits into four Stark levels, and the excited state, $^2F_{5/2}$ splits into three levels.[31] The

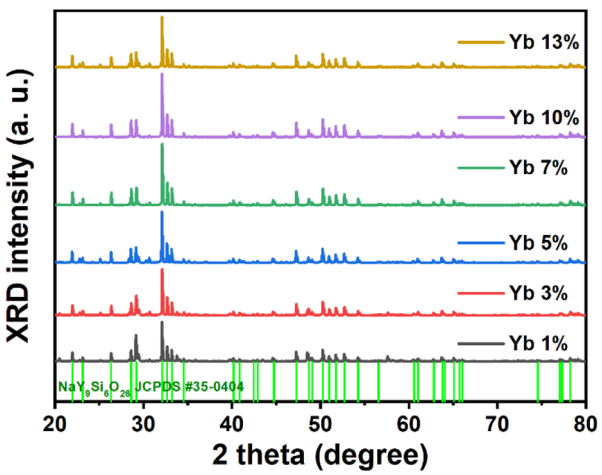

Fig. 2 XRD patterns of $NaY_9Si_6O_{26}$:Yb^{3+} phosphor doped with varying concentrations and $NaY_9Si_6O_{26}$ as reference (JCPDS #35-0404).

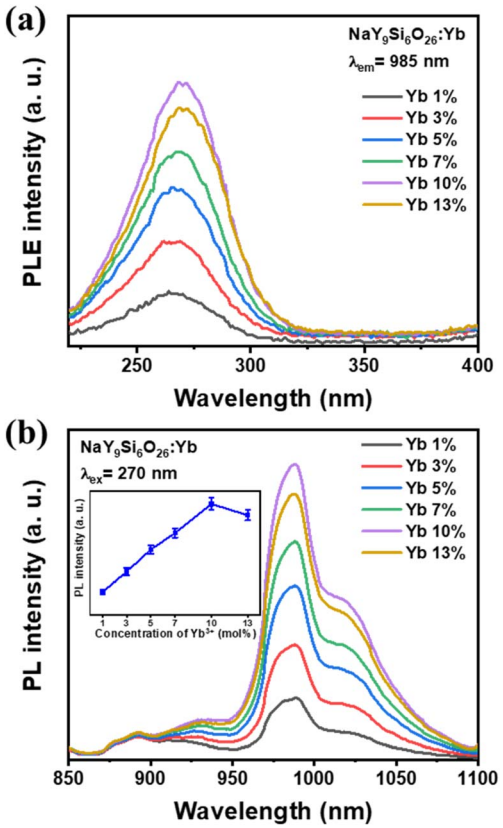

Fig. 3 (a) Excitation (λ_{em} = 985 nm), and (b) emission (λ_{ex} = 270 nm) spectra of $NaY_9Si_6O_{26}$:Yb^{3+} phosphors with varying concentrations of Yb^{3+} ions.

emission peak intensity of $NaY_9Si_6O_{26}$:Yb^{3+} phosphors increased with increasing Yb^{3+} concentration up to 10 mol% and then decreased, probably because of the concentration quenching effect.

In recent years, counterfeiting technology of security materials has advanced, making anti-counterfeiting technology an important tool for protecting the legitimate rights of consumers and enterprises.[32,33] It is therefore imperative to develop new materials for advanced anti-counterfeiting security. For this application, it is necessary to develop an NIR-emitting material that is sensitive in the NIR region beyond the existing method of checking security through ultraviolet excitation. In terms of security level, it can be applied to level 3 (forensic), which can be read only with dedicated equipment, beyond level 1, which can be visually identified, and level 2, which can be verified with general equipment. In order to explore the possibilities of these applications, the excitation and emission spectra of $NaY_9Si_6O_{26}$:Yb^{3+} phosphors in the NIR region and are shown in Fig. 4. The PLE spectra recorded by monitoring the emission at 985 nm exhibited a excitation band from 870 to 930 nm, as shown in Fig. 4(a). This can be attributed to the transition from the lowest ground state Stark level to the excited state Stark level in Yb^{3+} ions. In Fig. 4(b), the PL spectra of $NaY_9Si_6O_{26}$:Yb^{3+} phosphors excited at 920 nm show NIR emission from 960 to 1100 nm, which was attributed to the transition from the lowest Stark

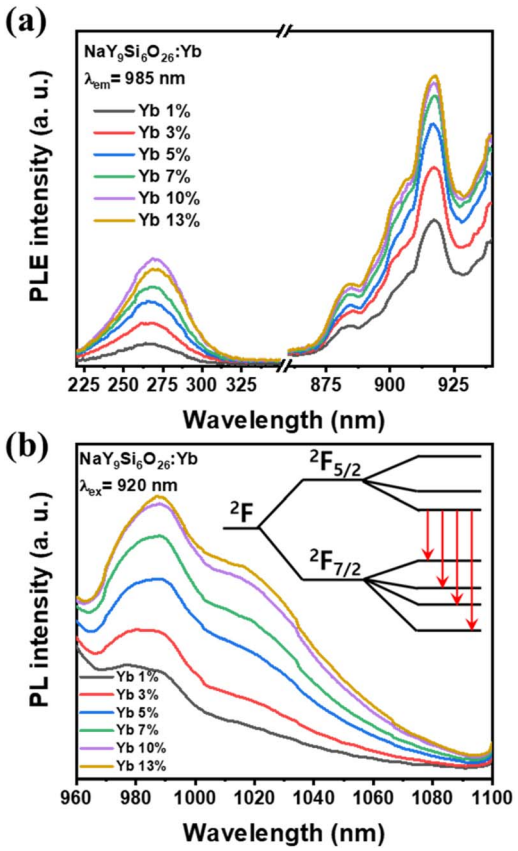

Fig. 4 (a) Excitation (λ_{em} = 985 nm), and (b) emission (λ_{ex} = 920 nm) spectra of $NaY_9Si_6O_{26}$:Yb^{3+} phosphors with varying concentrations of Yb^{3+} ions in NIR region.

level of $^2F_{5/2}$ to four Stark levels of the ground state $^2F_{7/2}$ in Yb^{3+} ions.

The thermal degradation behavior of NIR phosphors is an imperative factor for advanced anti-counterfeiting security because excellent thermal conductivity is necessary to employ the NIR emitting material in fiber application products (clothes, banknotes, passports, *etc.*). The temperature dependence of

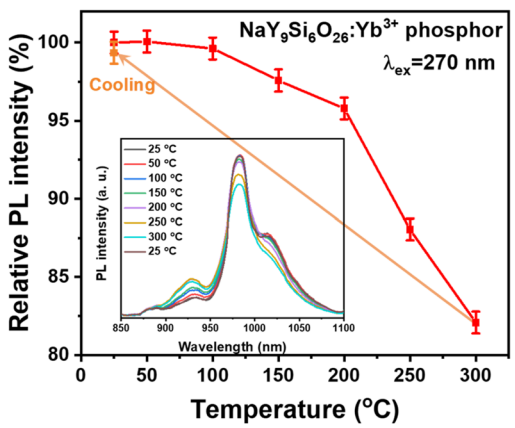

Fig. 5 Temperature dependence of the PL emission intensity of $NaY_9Si_6O_{26}$:Yb^{3+} phosphor. The inset shows the emission spectra.

$NaY_9Si_6O_{26}$:Yb^{3+} phosphor emission was measured to investigate its thermal stability. Fig. 5 shows the temperature-dependent PL intensity under 270 nm excitation in the temperature range 25–300 °C. The emission intensity of $NaY_9Si_6O_{26}$:Yb^{3+} phosphor decreased with increasing temperature. The relative PL intensity of $NaY_9Si_6O_{26}$:Yb^{3+} phosphor was 82% of the initial PL intensity at 300 °C, indicating its excellent thermal stability. Moreover, its thermal quenching behavior can be attributed to the non-radiative relaxation of thermally activated electron–phonon coupling.[34] Finally, after heating the $NaY_9Si_6O_{26}$:Yb^{3+} phosphor to 300 °C and then cooling to room temperature, the NIR emission intensity recovered nearly 100% of its initial intensity, indicating that thermal degradation was minimal. This suggests applicability to advanced anti-counterfeiting applications.

Conclusions

We developed the new NIR-emitting Yb^{3+}-doped $NaY_9Si_6O_{26}$ phosphors using conventional solid-state reaction. The synthesized phosphors showed a hexagonal crystal structure corresponding to the apatite compound with a small amount of yttrium silicate impurities. It showed angular-shaped fine grains with an average grain size of 1–3 μm. The PLE spectra of the $NaY_9Si_6O_{26}$:Yb^{3+} phosphors, monitored at an emission wavelength of 985 nm, showed two excitation bands, 220–300 nm and 870–970 nm, respectively. The former was attributed to the charge transfer transition of Yb^{3+} ions, and the latter was attributed to the transition from the lowest Stark level of the ground $^2F_{7/2}$ to three Stark levels of the excited $^2F_{5/2}$ in Yb^{3+} ions. The emission spectra under 270 and 920 nm excitation presented a NIR emission band from 950 to 1100 nm, which corresponds to the transition of Yb^{3+} ions from the lowest Stark level of the excited $^2F_{5/2}$ to four Stark levels of the ground $^2F_{7/2}$. These luminescent properties indicate that it can be used as a material in the security field that is sensitive to the NIR as well as the ultraviolet region. The excellent thermal stability of $NaY_9Si_6O_{26}$:Yb^{3+} phosphor was evident from the fact that the relative PL intensity of $NaY_9Si_6O_{26}$:Yb^{3+} phosphor was 82% of the initial PL intensity at 300 °C. The emission intensity that showed thermal quenching up to 300 °C recovered to its initial emission intensity when cooled to 25 °C. Thus, it was confirmed that a minimal amount of thermal degradation occurred. The results of our study suggest that $NaY_9Si_6O_{26}$:Yb^{3+} phosphors are promising next-generation candidates for advanced anti-counterfeiting applications.

Conflicts of interest

There are no conflicts to declare.

Acknowledgements

This work was supported by the Technology Innovation Program (20021925, Development of Environment-Friendly Security Fiber and Application Products Using Near-Infrared

Light Pigments Over 1000 nm) funded by the Ministry of Trade, Industry & Energy (MOTIE, Korea).

Notes and references

1 H. W. Siesler, Y. Ozaki, S. Kawata and H. M. Heise, *Near-Infrared Spectroscopy: Principles, Instruments, and Applications*, John Wiley & Sons, Germany, 2008.
2 Z. Y. Wang, *Near-Infrared Organic Materials and Emerging Applications*, CRC Press, Boca Raton, 2013.
3 K. Svoboda and S. M. Block, Biological Applications of Optical Forces, *Annu. Rev. Biophys. Biomol. Struct.*, 1994, **23**, 247–285.
4 M. Wolf, M. Ferrari and V. Quaresima, Progress of near-infrared spectroscopy and topography for brain and muscle clinical applications, *J. Biomed. Opt.*, 2007, **12**, 062104.
5 V. Ntziachristos, C. Bremer and R. Weissleder, Fluorescence imaging with near-infrared light: new technological advances that enable *in vivo* molecular imaging, *Eur. Radiol.*, 2003, **13**, 195.
6 V. Rajendran, H. Chang and R. S. Liu, Recent progress on broadband near-infrared phosphors-converted light-emitting diodes for future miniature spectrometers, *Opt. Mater.: X*, 2019, **1**, 100011.
7 V. Rajendran, M.-H. Fang, G. N. D. Guzman, T. Lesniewski, S. Mahlik, M. Grinberg, G. Leniec, S. M. Kaczmarek, Y.-S. Lin, K.-M. Lus, C.-M. Lin, H. Chang, S.-F. Hu and R.-S. Liu, Super broadband near-infrared phosphors with high radiant flux as future light sources for spectroscopy applications, *ACS Energy Lett.*, 2018, **3**, 2679.
8 D. Kim, Y. Jung, K.-A. Toh, B. Son and J. Kim, An empirical study on iris recognition in a mobile phone, *Expert Syst. Appl.*, 2016, **54**, 328.
9 R. Filippo, E. Taralli and M. Rajteri, LEDs: sources and intrinsically bandwidth-limited detectors, *Sensors*, 2017, **17**, 1673.
10 S. Fuchi and Y. Takeda, Wideband near-infrared phosphor by stacking Sm^{3+} doped glass underneath Yb^{3+}, Nd^{3+} co-doped glass, *Phys. Status Solidi C*, 2011, **8**, 2653.
11 Q. Shao, H. Ding, L. Yao, J. Xu, C. Liang and J. Jiang, Photoluminescence properties of a $ScBO_3$:Cr^{3+} phosphor and its applications for broadband near-infrared LEDs, *RSC Adv.*, 2018, **8**, 12035.
12 Q. Shao, H. Ding, L. Yao, J. Xu, C. Liang, Z. Li, Y. Dong and J. Jiang, Broadband near infrared light source derived from Cr^{3+}-doped phosphors and a blue LED chip, *Opt. Lett.*, 2018, **43**, 5251.
13 Z. Pan, Y.-Y. Lu and F. Liu, Sunlight-activated long-persistent luminescence in the near infrared from Cr^{3+}-doped zinc gallo germanates, *Nat. Mater.*, 2011, **11**, 58.
14 H. Zeng, T. Zhou, L. Wang and R. J. Xie, Two-site occupation for exploring ultrabroadband near-infrared phosphor—double-perovskite La_2MgZrO_6:Cr^{3+}, *Chem. Mater.*, 2019, **31**, 5245.
15 T. Gao, W. Zhuang, R. Liu, Y. Liu, C. Yan, J. Tian, G. Chen, X. Chen, Y. Zheng and L. Wang, Site occupancy and enhanced luminescence of broadband NIR gallo germanate phosphors by energy transfer, *J. Am. Ceram. Soc.*, 2019, **103**, 202.
16 Y. Zhong, S. Gai, M. Xia, S. Gu, Y. Zhang, X. Wu, J. Wang, N. Zhou and Z. Zhou, Enhancing quantum efficiency and tuning photoluminescence properties in far-redemitting phosphor $Ca_{14}Ga_{10}Zn_6O_{35}$:Mn^{4+} based on chemical unit engineering, *Chem. Eng. J.*, 2019, **374**, 381.
17 L. Zhang, D. Wang, Z. Hao, X. Zhang, G. h. Pan, H. Wu and J. Zhang, Cr^{3+}-doped broadband NIR garnet phosphor with enhanced luminescence and its application in NIR spectroscopy, *Adv. Opt. Mater.*, 2019, **7**, 1900185.
18 L. Sánchez-García, M. O. Ramírez, R. M. Solé, J. J. Carvajal, F. Díaz and L. E. Bausá, Plasmon-induced dual-wavelength operation in a Yb^{3+} laser, *Light Sci. Appl.*, 2019, **8**, 1.
19 B. T. Huy, D. H. Kwon, S. S. Lee, V. D. Dao, H. B. Truong and Y. I. Lee, Optical properties of Sr_2YF_7 material doped with Yb^{3+}, Er^{3+}, and Eu^{3+} ions for solar cell application, *J. Alloys Compd.*, 2022, **897**, 163189.
20 Y. Xu, L. Zhang, L. Dong, S. Yin, X. Wu and H. You, Novel $SrGd_2Al_2O_7$:Mn^{4+}, Nd^{3+}, and Yb^{3+} phosphors for c-Si solar cells, *Dalton Trans.*, 2021, **50**, 7017.
21 J. Miao, M. Chen, Z. Chen, L. Zhang, S. Wei and X. Yang, Effect of Yb^{3+} concentration on upconversion luminescence and optical thermometry sensitivity of La_2MoO_6: Yb^{3+}, Er^{3+} phosphors, *Appl. Opt.*, 2021, **60**, 1508.
22 S. Liu, H. Ming, J. Cui, S. Liu, W. You, X. Ye, Y. Yang, H. Nie and R. Wang, Color-tunable upconversion luminescence and multiple temperature sensing and optical heating properties of $Ba_3Y_4O_9$:Er^{3+}/Yb^{3+} phosphors, *J. Phys. Chem. C*, 2018, **122**, 16289.
23 K. Pavani, J. Suresh Kumar, K. Srikanth, M. J. Soares, E. Pereira, A. J. Neves and M. P. E. Graca, Highly efficient upconversion of Er^{3+} in Yb^{3+} codoped non-cytotoxic strontium lanthanum aluminate phosphor for low temperature sensors, *Sci. Rep.*, 2017, **7**, 17646.
24 D. K. Zharkov, A. G. Shmelev, A. V. Leontyev, V. G. Nikiforov, V. S. Lobkov, M. H. Alkahtani, P. R. Hemmer and V. V. Samartsev, Light converting Yb^{3+}/Er^{3+} doped YVO_4 nanoparticles for biological applications, *Laser Phys. Lett.*, 2020, **17**, 075901.
25 M. Shang, D. Geng, D. Yang, X. Kang, Y. Zhang and J. Lin, Luminescence and Energy Transfer Properties of $Ca_2Ba_3(PO_4)_3Cl$ and $Ca_2Ba_3(PO_4)_3Cl$:A (A = Eu^{2+}/Ce^{3+}/Dy^{3+}/Tb^{3+}) under UV and Low-Voltage Electron Beam Excitation, *Inorg. Chem.*, 2013, **52**, 3102.
26 L. Wang, B. K. Moon, B. C. Choi, J. H. Kim, J. Shi and J. H. Jeong, Photoluminescent properties and site occupation preference in Bi^{3+}, Eu^{3+} doped $CaY_4(SiO_4)_3O$ phosphor, *Ceram. Int.*, 2016, **42**, 12971.
27 W. Zhou, F. Pan, L. Zhou, D. Hou, Y. Huang, Y. Tao and H. Liang, Site Occupancies, Luminescence, and Thermometric Properties of $LiY_9(SiO_4)_6O_2$:Ce^{3+} Phosphors, *Inorg. Chem.*, 2016, **55**, 10415.
28 G. R. Redhammer and G. Roth, Lithium and Sodium Yttrium Orthosilicate Oxyapatite, $LiY_9(SiO_4)_6O_2$ and $NaY_9(SiO_4)_6O_2$, at Both 100 K and Near Room Temperature, *Acta Crystallogr.*, 2003, **59**, i120.

29 K. Momma and F. Izumi, VESTA: a three-dimensional visualization system for electronic and structural analysis, *J. Appl. Crystallogr.*, 2008, **41**, 653.
30 G. Blasse and B. C. Grabmaier, *Luminescent Materials*, Springer, Heidelberg, 1994.
31 L. Sánchez-García, M. O. Ramírez, C. Tserkezis, R. Sole, J. J. Carvajal, M. Aguiló, F. Díaz and L. E. Bausá, Anisotropic Enhancement of Yb^{3+} Luminescence by Disordered Plasmonic Networks Self assembled on $RbTiOPO_4$ Ferroelectric Crystals, *Nanoscale*, 2017, **9**, 16166.
32 G. Cai, T. Delgado, C. Richard and B. Viana, ZGSO Spinel Nanoparticles with Dual Emission of NIR Persistent Luminescence for Anti-Counterfeiting Applications, *Materials*, 2023, **16**, 1132.
33 Y. Xiao, P. Xiong, S. Zhang, K. Chen, S. Tian, Y. Sun, P. Shao, K. Qin, M. G. Brik, S. Ye, D. Chen and Z. Yang, Deep-red to NIR mechanoluminescence in centrosymmetric perovskite $MgGeO_3$: Mn^{2+} for potential dynamic signature anti-counterfeiting, *Chem. Eng. J.*, 2023, **453**, 139671.
34 M. Kaczkan, M. Malinowski, A. Suchocki, D. A. Pawlak and S. Turczyński, Temperature and concentration dependent luminescence of Yb^{3+} centers in YAM, *J. Alloys Compd.*, 2020, **842**, 155893.